Turbine tent measurements of marine hydrocarbon seeps on subhourly timescales

Ira Leifer
Marine Sciences Institute, University of California, Santa Barbara, California, USA

Jim Boles
Department of Geological Sciences, University of California, Santa Barbara, California, USA

Received 16 November 2003; revised 9 July 2004; accepted 16 August 2004; published 28 January 2005.

[1] Three turbine seep-tents simultaneously measured marine seep gas fluxes with high time resolution (0.2 s) at multiple locations. Tents were inverted polyvinyl cones, 2-m diameter, 1-m tall, and weighted on their lower skirt edges. Rising gas bubbles induce vertical fluid motions, which were measured by laboratory-calibrated turbines in chimneys on top of the tents. Initial deployment was at an active seep area in the Coal Oil Point seep field, in the Santa Barbara Channel, California. The three tents simultaneously collected data for continuous time periods of 2 hours in both the morning and afternoon. Seabed temperature and pressure were acquired every 3 s over the same time periods as the flux measurements from a conductivity temperature depth, CTD, mounted on one tent. Results strongly suggest that oceanic swell had a significant forcing effect on the flux at a subhourly timescale. There was an inverse relationship between effect of swell height on the flux and flux. Swells from 1 to 4 m height and periodicities of 7 and 12 s caused variations of ~1% to 4% from the average flux. Proposed mechanisms to explain the observations are diffusion with surrounding sediments, termed gas charging, swell induced changes in fracture size, termed fracture forcing, and swell induced vent activation/deactivation, termed pore activation. On the basis of the seep frequency response, we propose pore activation was dominant.

Citation: Leifer, I., and J. Boles (2005), Turbine tent measurements of marine hydrocarbon seeps on subhourly timescales, *J. Geophys. Res.*, *110*, C01006, doi:10.1029/2003JC002207.

1. Introduction

[2] Hydrocarbon (HC) seeps represent an important pathway by which natural gases, primarily methane, leak from the lithosphere into the hydrosphere and atmosphere. Methane is an important greenhouse gas, and seep emissions are comparable to other sources, such as termites [*Khalil and Rasmussen*, 1995]. Recent global methane flux estimates conservatively suggest 35–45 Tg yr^{-1} from both terrestrial and marine sources, i.e., approximately 7% of the global atmospheric methane budget (540 Tg yr^{-1}) [*Prather et al.*, 1995]. Of this flux, the marine contribution is estimated at 20 Tg yr^{-1} [*Kvenvolden et al.*, 2001] and arises primarily from seeps (hydrate and thermogenic); however, there are significant uncertainties since few quantitative values for seepage flux exist. Furthermore, most of the existing measurements do not address temporal or spatial variations in these highly dynamic systems. For example, seeps vary on timescales from the tidal to decadal [*Tryon et al.*, 1999; *Boles et al.*, 2001].

[3] *Boles et al.* [2001] reported that the flux from two large, steel seep-tents (each 30 m by 30 m) in the Santa Barbara Channel had variations driven by tidal frequencies. The flux data were collected from two large steel tents placed over a very active seep area off Coal Oil Point in water ~70 m deep. At the time, the seep tents produced a minimum of 16,800 m^3 d^{-1} of methane. The hourly averaged flux over a 9-month period showed a clear inverse correlation between tide height and flux. A 1-m increase in tide height resulted in a ~2% decrease in flux. *Boles et al.* [2001] proposed a pore activation model to explain these observations in which an increase in pressure shuts off flow from small pores/fractures because the gas within the pore/fracture cannot overcome the increased external hydrostatic pressure to escape the vent mouth.

[4] In this paper we present observations from a new flux measurement device on a timescale comparable to ocean swell-induced hydrostatic pressure changes, i.e., order ~10 s. This data was collected in a shallow (~22 m deep) area of very active seepage in the Santa Barbara Channel, California. Aside from demonstrating a new response characteristic of seeps, these measurements provide a tool to probe subsurface structure and flows. The response of the seep flux to hydrostatic pressure changes

Copyright 2005 by the American Geophysical Union.
0148-0227/05/2003JC002207$09.00

is related to the subsurface structure. Moreover, different frequencies probe different portions of the seep, i.e., shorter period swell induces a response in shallower portions of the seep than longer period swell.

2. Turbine Seep-Tent

2.1. Theory of the Turbine

[5] The physical process that causes the turbine to rotate is the buoyancy-driven upwelling flow in the water. Dye was injected directly in front of large bubbles rising into the turbine and imaged with a high-speed video camera (Figure 1) to visualize these motions. Rising bubbles push water in front of them (bow wave) and accelerate fluid behind them in a turbulent wake (for bubbles whose rise is nonlaminar, i.e., $r > \sim 300$ μm, where r is the equivalent spherical bubble radius). The bubbles lose momentum to the surrounding fluid by these two flows, primarily through the wake rather than the bow wave. The wake can persist for order of 100 s, so given a sufficiently high density of bubbles, the wakes associated with each bubble merge, creating an upwelling flow. The upwelling flow has long been known in chemical engineering [*Hills*, 1974; *Chen et al.*, 1994] where in chemical reactors (walls) it has high spatial and temporal variability.

[6] Since bubble wake development is strongly dependent on bubble size [*Fan and Tsuchiya*, 1990], the associated fluid motions induced by a single bubble are also strongly size dependent [*Leifer and Patro*, 2002]. As a result, the total upwelling flow driving a turbine depends upon the bubble-size distribution at the turbine (coalescence in the tent may change the size distribution). One approach to the problem of a bubble-size dependent spin rate for a given flow is to use a bubble breakup-grid to ensure all bubbles are roughly the same size over a wide range of fluxes.

[7] Several forces are at work that convert the vertical flow into turbine rotation, thereby affecting the design. Below the turbine, the fluid and bubble velocities are vertical. If the turbine is stationary, the buoyancy force acts on a solid body and the turbine blade experiences a three-component force, vertically, toward the turbine axis, and in the turbine's rotational direction. Naturally, only the latter contributes toward turbine rotation. Lets consider two extreme cases of blade tilt. In the case of a very shallow blade (e.g., an Archimedes screw), the upwelling flow's force is primarily vertical with a small component in the rotational direction. As a result, the upwelling flow rapidly decelerates as it loses most of its energy pushing vertically on the turbine blade. Furthermore, the rotational force must be sufficient to overcome turbine inertia, thus the shallower the blade angle to the flow, the lower the sensitivity. Conversely, if the blades are very steep, they have less effect on the flow (deceleration) and the turbine responds quicker. However, since the upwelling force is from a fluid, both Cartesian and rotational fluid motions are generated. Thus, there is a competition between fluid translation and generation of a force on the blade. While the blade mass is minimal, blade movement (rotation) requires displacement of significant water mass. Thus, if the blades are too steep, most of the upwelling flow's force translates the fluid around the blades.

[8] Since the bubble-driven upwelling flow vertically transports mass, continuity dictates the existence of a replacement flow. There are only two possible replacement flows, either downward through the turbine or under the tent bottom. A flow visualization study similar to that shown in Figure 1 showed the upwelling flow was along the turbine blades lower surface. During the field deployment the return flow must have been through the turbine since the tent was "sealed" against the mud-sand seabed on which its lower skirt rested. Thus the return flow must be along the blades' upper surface. This return flow creates a force that opposes the turbine spin from the upwelling flow.

[9] The turbine-bubble-flow interaction is more complex for the typical situation of a spinning turbine. In this case, the upwelling flow slows the spin when it enters the turbine since it contains fluid that must be accelerated to the turbine's spin speed (i.e., angular momentum is added to the flow). Then when the flow reaches the turbine blade it accelerates the turbine. Thus, the turbine spin rate at any moment represents the integrated effect (positive and negative) of all bubbles rising through the turbine, and the minimum response time is (to first order) the time for bubbles to rise 1/2 the blade height. For the turbine described herein, this was $\sim$0.1 s (3 cm/30 cm s^{-1}). For higher time resolution, the turbine begins to resolve the trajectory of the bubbly flow through the turbine, which was observed in the high-speed video. Another aspect is that since the turbine responds to the upwelling flow rather than the bubbles, large but brief bubble pulses become spread out in time. This was demonstrated by large bubble pulses ($\sim$1 liter in 0.2 s) produced in the laboratory. The turbine began spinning $\sim$0.5 s before the bubbles' arrival (bow wave) and continued spinning for many seconds after the bubble pulse passed (wake).

2.2. Description

[10] The turbine seep-tent (Figure 2) contained a turbine located in a chimney whose rotation is related to the gas flux through the tent. The turbine was machined out of a polyvinyl chloride (PVC) block with 4 blades tilted at 45°. As a result, all vertical paths through the turbine (i.e., that of rising bubbles) intersect a blade surface. The outer far edges of the turbine blades were parallel to the chimney wall with $\sim$1 mm clearance to the wall. The chimney was clear acrylic to allow visual inspection of the turbine, thereby assuring that it was not debris blocked (primarily a concern during deployment). The turbine had a 2-cm diameter central axle with internal glass bearings in ultra high molecular weight plastic races to minimize friction without lubrication. For the deployed tents, the spin rate was detected by four magnets on the axle that rotated past a Hall Effect sensor, generating four pulses per rotation. The turbine was mounted in the chimney by four arms that were secured by elastic straps and aluminum clips. This arrangement facilitated deployment and allowed the turbine to "pop" off the tent, rather than break if strongly pushed (by a gas ejection) or tugged (by the cable). In such case, the elastic lines snapped and were easily replaced.

[11] The chimney was connected to a 2-m diameter, 1-m tall, inverted conical tent made from pop-riveted 1/16-inch thick PVC sheets. The cone also was riveted to a support frame of 1/2-inch diameter PVC plastic pipes. The bottom

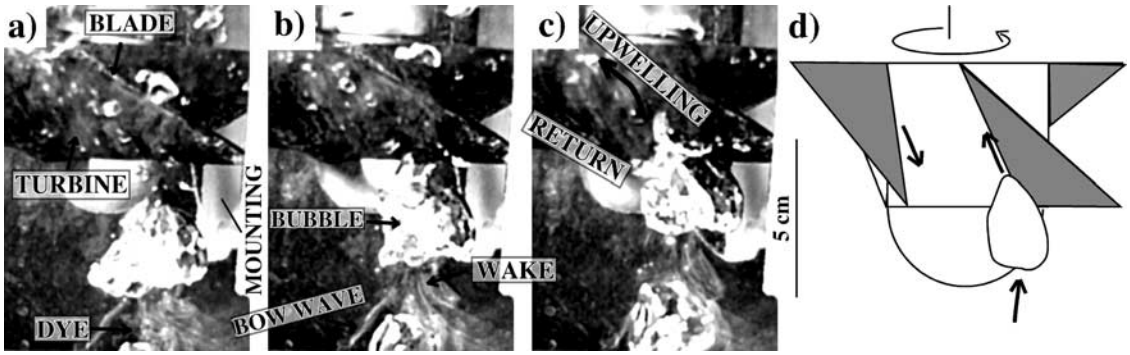

Figure 1. (a–c) Flow visualization images from high-speed image sequence (Kodak, Ektapro) of the turbine in a small glass tank with fluorescein dye injection and (d) schematic of turbine shown in Figures 1a–1c. Video frame rate was 125 frames per second, and each panel represents a five frame interval. Size scale on rightmost panel.

support frame was a PVC pipe loop that was attached to the tent plastic by a rope threaded through a series of holes at the tent's bottom edge. The deployment bridle was attached to three eyebolts in the pipe loop as well as five 2-kg diving weights distributed around the loop. This arrangement evenly distributed stress during recovery when the tents acted like sea anchors. The tents sat directly on the seabed. The tent and turbine design minimized costs to maximize the number of tents in the network.

[12] Internal to the tent and ~30 cm below the chimney was a metal screen grid that broke rising bubbles and blocked debris and fauna from entering the turbine and entangling the blades. A 0.32-cm grid size was chosen after testing as best for bubble breakup without noticeable gas retention. Smaller grid sizes caused bubble accumulation, with the result that a steady gas flow became pulsed. Larger screens functioned poorly at bubble breakup with bubbles immediately recoalescing above the screen.

[13] The Hall Effect sensors were connected to a multichannel data logger (OMP-MODL, Omega, Stamford, Connecticut) by an underwater three-conductor (power, ground, signal) cable with attached rope strain reliefs. The Hall Effect sensors require a DC voltage input while their output is a series of pulses that the data logger recorded. The data logger can be deployed on the seabed or on an onsite ship and was configured to record the number of pulses per time interval. The interval was set as short as possible to provide the highest time resolution. Unfortunately, this introduced a quantization noise that complicated data analysis. An alternate approach is to record the time between pulses, but this produces data that is more difficult to compress. Although the data logger can record 500,000 samples (8 channels), for a 1-s time interval, this is equivalent to only ~5 days; thus compression is critical.

2.3. Calibration

[14] The system was calibrated in a small and large tank. The small tank volume was 40 L and glass, while the large tank was the UCSB Ocean Engineering Laboratory wind-wave channel, which is 3-m deep, 5-m wide, and 52-m long. Bubbles were created by connecting an air compressor to a regulator and then through one of a series of rotameter/flow controllers spanning 5 $cm^3\ s^{-1}$ to 23,600 $cm^3\ s^{-1}$ (FL3840C, FL31615A, FL-3804ST, HFL2709A, HFL6760A, Omega Engineering, Stamford, Connecticut). An air tube ran from the controllers to the tank bottom where it was connected to one of two air stones or a 1-cm diameter hose without an attached air stone. The open-

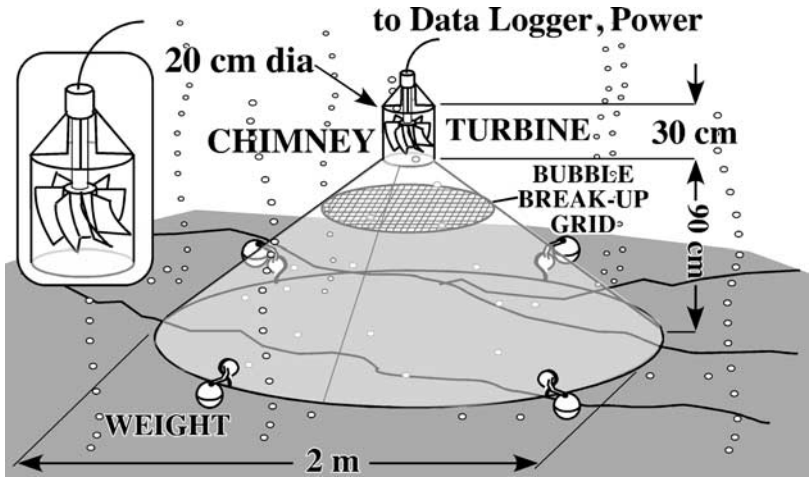

Figure 2. Turbine seep-tent schematic. Inset shows turbine details.

ended tube produced pulses of very large (2- to 5-cm diameter) bubbles. One air stone produced many large bubbles ~0.5-cm diameter, while the other air stone produced much smaller bubbles. Although precise size distributions were not measured, the three bubble sources spanned a wider range of sizes than typically observed at the field deployment site [*Leifer and Boles*, 2004].

[15] The tent was placed on top of the bubble source and connected to the data logger. Flow rates were measured from a highly magnified view of the controllers by a CCD video camera. At each flow setting, turbine rotation rates were measured for several minutes. The measured rates were averaged and the error (1 standard deviation) calculated. Flow rates were corrected using Boyle's law, $V_1 = P_2V_2/P_1$, for the hydrostatic pressure, P, at the turbine depth (P_1) for bubbles produced at the air stone depth (P_2), where V_1 and V_2 are the gas volume flows (per second) at the turbine and at the air stone depth, respectively. The rotameter measured V_2. Calibration experiments investigated the effects of the bubble-size distribution, tent angle from vertical, location within the tent of the bubble stream, and the effect of the chimney wall. For the latter, the turbine was mounted in the small glass tank without the tent or chimney.

[16] Results from the calibration experiments are shown in Figure 3. The effect of the walls on turbine spin is shown clearly by the higher rotation rates without the tent (squares) as compared to with the tent (diamonds and circles) for the same flow. The fit for the large tank calibration data over the range indicated by the dashed line was

$$F = 104.42*R^{1.82}, \quad (1)$$

where F is gas flow (L s^{-1}) and R is rotation rate (revolutions per second) with a correlation coefficient of 0.985 for $R > 0.3$ and all three bubble sources. At the lowest flow rates, friction, viscous damping, and inertia were likely responsible for the rapid decrease in the turbine response (when the turbine stopped for very low flow, the upwelling flow was not always able to restart it spinning immediately). The calibration was insensitive to location of the bubble source in the tent (i.e., at an edge, or under the apex). If the turbine was tilted too much, the rotation rate decreased causing an error (Figure 3b), but the effect was negligible (0–2.5%) for small angles (0°–5°). A quadratic fit described the tilting effect quite well up to 17°, after which bubbles began spilling from the tent edge. The fit was

$$\varepsilon = 0.1537\alpha^2 - 0.2750\alpha + 0.0789, \quad (2)$$

where α is the angle from vertical (°), and ε is the error in F (%).

[17] One calibration series was for the tent suspended 2 m above the bubble source (empty circles), which also produced higher rotation rates, particularly at the lower flow rates. However, the similarity of the data for $F >$ 200 cm^3 s^{-1} shows that the upwelling flow achieved near steady state within less than the tent height for higher flows. Furthermore, the wire grid was unlikely to have significantly affected the upwelling flow, for example, there was no indication of bubble retention at the grid, i.e., bubbles easily pass the grid and thus the upwelling flow also should pass easily. Postmission calibration (not shown) agreed well with the premission values.

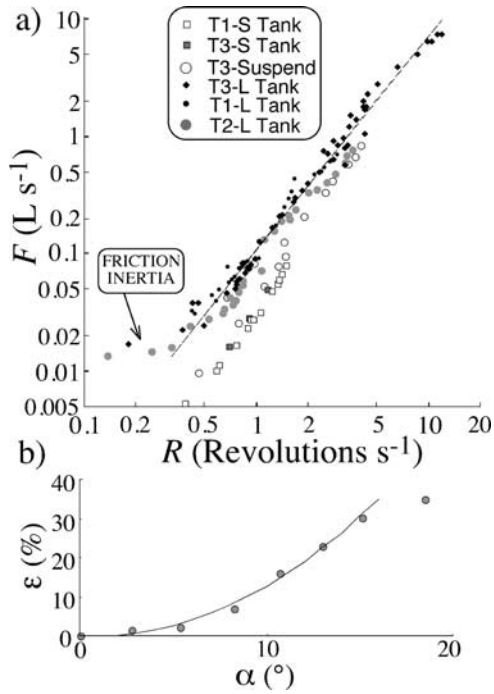

Figure 3. (a) Calibration of turbine rotation rate, R, with flow rate, F (L s^{-1}). Abbreviations are as follows: T1, small-bubble air stone; T2, large-bubble air stone; T3, no air stone. Also shown is the least squares, linear regression analysis fit to data collected with the tent in the channel over the range of the fit. Error bars are 1 standard deviation. "Suspend" is for tent suspended a meter above the air stone, L is for large and S is for small tank. (b) Error, ε (%), versus tent angle from vertical, α (deg). For further details, see text. Data key is shown in Figure 3a.

3. Field Deployment

3.1. Site Description

[18] Scuba-equipped divers deployed the tents on 11 March 2003 at an active seep area, Shane Seep (34°24.370′N, 119°53.428′W) in the Coal Oil Point (COP) seep field, Santa Barbara Channel, California (Figure 4). The northern margin of the Santa Barbara Channel is one of the most active areas of natural hydrocarbon seepage in the world [*Hornafius et al.*, 1999]. The largest seepage is in moderately shallow water (20–100 m) a few kilometers from the University of California, Santa Barbara. Current estimates from both flux buoy surveys and sonar surveys suggest that ~1.5 × 10^5 m^3 d^{-1} (5 × 10^6 cubic feet per day) of gas escapes from these seeps to the atmosphere [*Hornafius et al.*, 1999; *Clark et al.*, 2003] with roughly an equal amount injected into the coastal ocean [*Clark et al.*, 2000]. Oil discharge estimates range from 6800 to 33,000 L d^{-1} (40 to 200 barrels per day) [*Allen et al.*, 1970; *Clester et al.*, 1996; *Hornafius et al.*, 1999]. There are no published estimates for tar released into the channel waters or its shallow sediment.

[19] Shane Seep has been the focus of intensive investigations for several years, including bubble distributions

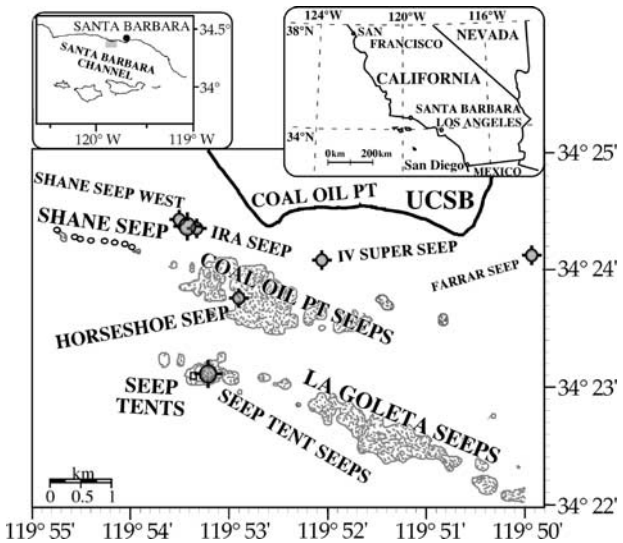

Figure 4. Location of informally named seeps in the Coal Oil Point seep field, Santa Barbara Channel. Top right panel shows the southwest U.S. coast; top left panel shows the Santa Barbara Channel with gray rectangle indicating the location of the study area, shown in bottom panel. Gray areas in bottom panel indicate regions of high bubble density from sonar returns [*Hornafius et al.*, 1999]. Inshore seeps (Shane Seep, IV Super seep, and Farrar Seep) were too shallow for the sonar survey.

and bubble plume dynamics [*Leifer et al.*, 2000; *Leifer and Boles*, 2004], oil and tar characterization and microbial community structure [*La Montagne et al.*, 2004], seabed morphology [*Leifer et al.*, 2004], biological fauna surveys (unpublished), and gas flux measurements. Flux measurements at Shane Seep by a direct-capture flux-buoy device, recorded some of the highest flux values per square meter for the entire COP seep field [*Clark et al.*, 2003].

[20] Major seabed features were surveyed on 11 March 2003 by scuba-equipped divers using measuring tapes, levels, and underwater video (Figure 5). In November 2001, two heavy iron chains, each 17-m long, were laid on the seabed along north-south and east-west transects. Several hundred kilograms of metal was placed at the intersection as a mooring point and a spar buoy attached. At the time of tent deployment, the seabed was characterized by three main vents (1–3) located in two primary hydrocarbon (HC) volcanoes. The HC volcanoes are so termed because the volcano walls are primarily tar and sand [*La Montagne et al.*, 2004] rather than mud. For a discussion of the changes in these seabed features over several years, see *Leifer et al.* [2004].

[21] Intense seepage also was observed at the mooring point (vent 0), although much less than from vents 1–3. The east-west transect chain passed through the walls of HC volcano 3, while elsewhere it had not appreciably sunk into the sediment over the several years since deployment. The east-west alignment of the main vents strongly suggests control by an underlying east-west fracture structure, as is typical in this area [*Hornafius et al.*, 1999]. A push core the prior year in HC volcano 1 indicated a layer about 30 cm thick of mixed HC, sediment, and sand overlying a sand layer, although the sand overburden likely varies with storms and season. The sediment overburden in this region is ~2 m (B. Luyendyk, University of California, Santa Barbara, personal communication, 2003) and overlies fractured Monterey shale [*Fischer*, 1978].

[22] The central seep zone contained the main vents, extending a few meters further south and north, and was characterized by numerous small vents located 30 to 50 cm apart. These vents predominantly produced streams of bubbles in lines. Outside this zone, in a region termed the "peripheral seep zone," vent density decreased, extending furthest toward the north-northeast and the south, to a distance of 10 to 13 m. In this outer area, vents were ~1–2 m apart and also produced rising lines of bubbles. Swell was visible at the seabed from sediment motion and some of the bubble lines appeared to temporarily deactivate in relationship to the swell, in agreement with the data presented below. Bacterial mats, primarily *Beggiatoa*, were common throughout the region, thickening near main vent openings where bacterial strand lengths reach ~0.5 cm.

[23] Tents were deployed in the peripheral zone in three areas of different seepage (Figure 5). The seabed was flat at these sites and the tents largely were flush with the seabed, thus their interiors were isolated from the surrounding ocean. A conductivity temperature depth, CTD (Model SB-39, Seabird, Florida), was attached to a supporting spar on one of the tents, ~70 cm above the seabed. The main HC volcanoes were avoided from a concern that the flux could lift them off the seabed.

3.2. Conditions

[24] The tents were deployed under calm seas (southerly swell ~1 m) and sunny skies. By late morning, a marine layer began moving into the region, arriving at about 1230 LT and accompanied by an increase in wind and swell. A second swell of shorter period than the southerly swell began arriving from the west. By midafternoon it began raining, waves were ~3 to 4 m and winds had increased further. At this time the tents were recovered and we returned to port.

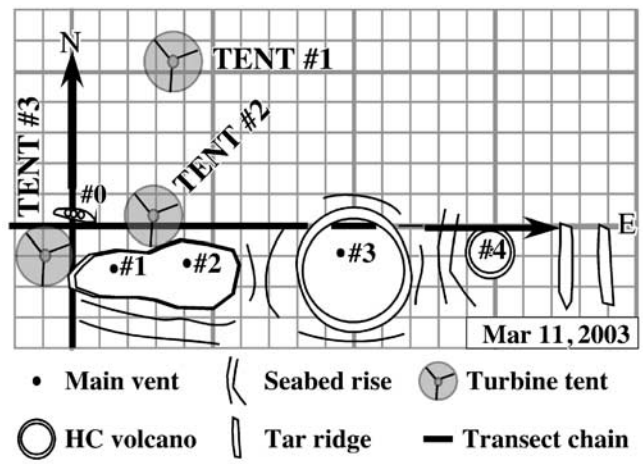

Figure 5. Seabed turbine tent deployment locations and major features at Shane Seep as measured during a seabed survey 11 March 2003. Major squares are 5 m; minor squares are 1 m. Symbol key on figure.

[25] Conditions recorded at the NOAA East Santa Barbara Buoy (Buoy 46053, 34°14.10′N, 119°51.00′W (data available at http://ndbc.noaa.gov/station_page.php?station=46053) show the changing weather during the day (Figure 6). Since the buoy was 19.40 km distant from the deployment site and weather and wave conditions often vary significantly over distances of just a kilometer or two in the channel, a CTD also was deployed at Shane Seep on one of the tents. The CTD showed that changes due to the storm arrived at the NOAA buoy significantly earlier than at Shane Seep. Early in the day, the dominant wave period at the NOAA buoy was (to the nearest second) 6 s, but by late in the day was 12 s. The CTD confirmed the relevance of the buoy wave spectra to conditions at Shane Seep by also showing two peaks in the wave spectra at 7 s and 12 s (Figure 6c). Unfortunately, the 7 s peak was close to the CTD Nyquist frequency (half the sample frequency), which recorded pressure signals each 3 s. Thus the NOAA buoy confirmed the 6–7 s period component of the swell. The NOAA buoy showed that during this time, the significant wave height (highest one third of all wave heights during the 20-min sampling period) increased from 0.9 to 1.6 m, while the atmospheric pressure fell ~3 mbar (0.3%). The water temperature decreased, while the air temperature initially increased with the normal diurnal cycle, before falling at 11 March 2003, 1200 LT due to the storm. There was also a long period swell of 18–19 s that increased in strength during the day.

[26] The CTD recorded the vertical temperature profiles during deployment and recovery. The average of all data within each 1-m depth layer is shown in Figure 7a. Also shown is the CTD record at the seabed during the day (Figure 7b). The tents were deployed at 1035 LT at which time the vertical temperature profile showed a well-mixed water column with a thin cold layer at the bottom. At ~1100 LT, scuba-equipped divers positioned the tents to the locations shown in Figure 5 and attached the turbines to the tent chimneys. Data collection began a few minutes later and is indicated by the labeled horizontal bars on Figure 7b. At 1310 LT, the shifting tide moved the boat, causing the turbines to pop off the chimneys (a design feature). The tide shift also was associated with an influx of colder water at the seabed. Approximately 1 hour after the tent data streams stopped, the divers returned to the seabed and replaced the turbines on the tents. Data collection continued for another 90 min, after which the tents were retrieved (divers retrieved the turbines, while the tents were hoisted by their bridles) due to the rapidly worsening weather. The vertical profile during recovery was dramatically different from deployment, with the deeper half of the water column cooler by up to a degree centigrade.

3.3. Observations

[27] The data logger recorded the number of pulses (4 per rotation) during each 0.2-s time interval. While providing very high time resolution data, since spin rates were ~2 revolutions s^{-1}, data were highly quantized. Using routines in MatLab (Mathworks, Massachusetts), raw data were first running averaged (1 s) and then block summed (1 s) to remove the quantization effect, but also reducing the time resolution. Revolution rates then were converted to a flux using the calibration function (1) and further corrected to standard temperature and pressure using the ideal gas law. Tent tilt was at most 1°–2°. Data from 1110 LT for both Tents 1 and 3 showed a generally decreasing flux trend, while Tent 2 was approximately constant (Figure 8). Close inspection of the flux records (Figures 8d–8f) shows a wave-like variation for all tents with an amplitude of ~10% the running averaged flux and with ~6 cycles per minute. Table 1 provides a summary of the data from the tents.

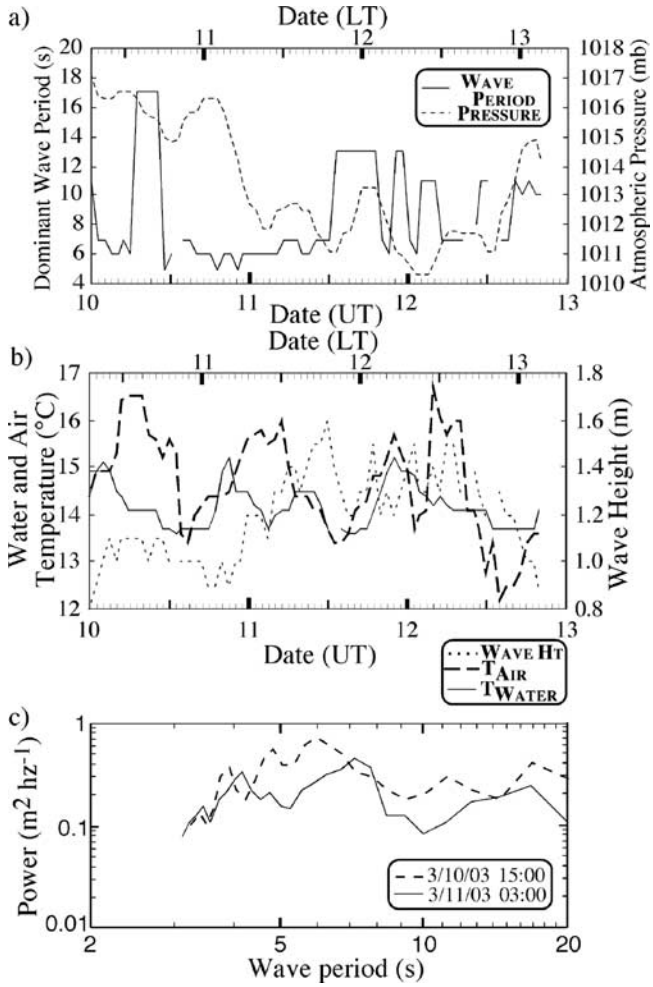

Figure 6. Data from NOAA buoy 46053 (E. Santa Barbara Channel), 19.4 km from Shane Seep. Bottom horizontal axis shows universal time; top shows local (Pacific daylight savings) time. (a) Dominant wave period and atmospheric pressure. (b) Water and air temperature, and wave height. (c) Power spectra for 11 March 2003, morning and afternoon. Data key on figure.

[28] To study these wave-like temporal variations further, the data series were detrended and power spectra calculated using a square window, which produces minimal spreading and decreasing of spectral peaks. For each tent, the average of a series of 1024-point power spectra with 50% overlap was calculated (Figure 9). Spectra were calculated for the morning (1110–1240 LT) and afternoon (1410–1540 LT). In the morning, the highest flow tent, Tent 1, had a dominant peak at 12.2 s, the other two tents had a peak within 0.1 s of Tent 1. However, the other two tents also showed a peak in the 6.5 s to 7.1 s range. For Tent 2, this

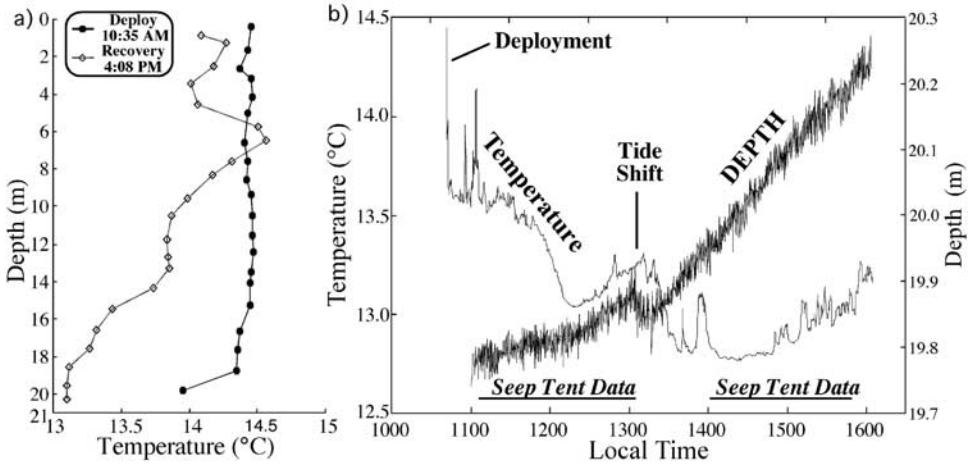

Figure 7. (a) Vertical temperature profiles and (b) seabed temperature and water depth for 11 March 2003, from the CTD mounted on one of the tents. Times of deployment, tide shift, and turbine data acquisition shown on Figure 7b. Data key is shown in Figure 7a; data are labeled in Figure 7b.

peak was actually stronger than the 12.2 s peak. By the afternoon, the short peak at 6.7 s was much stronger, and now was visible in Tent 1. Meanwhile, the 12.2 s peak had decreased to 11.5 s for the three tents, and had strengthened considerably, nearly an order of magnitude.

[29] Given that the dominant wave periods were 6 and 12 s (Figure 6c), the most probable driving force for these flux variations in the tents was swell. The spectra for the CTD pressure at Shane Seep in the morning and afternoon are shown in Figure 10. A clear and dominant peak is visible at 12 s, as is a second peak at 7 s. The other change in the pressure signal during the day was a growth in longer frequency components, particularly from 40 to 175 s. There was no clear evidence of a response to these longer period waves in the presented tent spectra (Figure 9). The other change was an increase in the strength of the 7 s peak.

4. Discussion

[30] The presented spectra show a response to swell. Seabed pressure variations due to swell were ~8.2 mbar (1 standard deviation of the detrended pressure data) for the morning, rising to ~8.6 mbar after ~1500 LT. This was an increase of ~0.013% of the total hydrostatic pressure (0.4 mbar/3 bar). The same trend of increasing variability was observed in the tent fluxes, with morning variations of 0.9%, 4.0%, and 1.5% for Tents 1–3, respectively, increasing to 1.1%, 4.3%, and 2.0% in the afternoon for Tents 1–3, respectively. Thus the seep flux variations were amplified from 20 to 100 times the wave-induced hydrostatic pressure variations, with the amplification depending upon the vent flux magnitude. These numbers also show that a 4.9% increase in variability (0.4 mbar) during the day from increasing wave height, caused a 7–33% increase in seepage variability, strongly suggesting nonlinearity in the seep response amplification of pressure variations.

[31] It is important to keep in mind that flux at each tent is the integrated flux of all vents underneath which span a range of vent sizes, shapes, and fluxes. Thus the tent response is an integration of the responses of the individual vents. Bigger vent mouths produce bigger bubbles [*Blanchard and Syzdek*, 1977], while mouths with

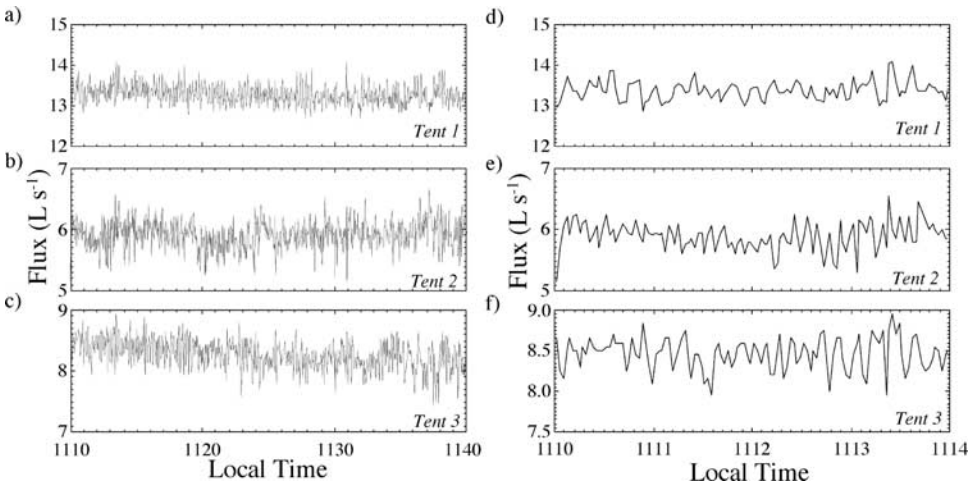

Figure 8. (a–c) The 30-min data set from Tents 1, 2, and 3 and (d–f) the first 4 min. Tents labeled in Figures 8a–8f.

Table 1. Summary of Characteristics of Turbine Seep-Tents[a]

Tent	Flow, L s^{-1}	σ (AM)	σ (PM)	Δ, %	Pk_1 (AM), s	Pk_2 (AM), s	Pk_2 (PM), s	Pk_2 (PM), s
1	13	0.9	1.1	22	...	12.2	6.7	11.5
2	5.7	4	4.3	2.5	6.5/7	12.3	6.7	11.6
3	8	1.5	2	33	7.1	12.1	6.7	11.5

[a]Δσ is standard deviation; Δ = σ(PM)/σ(AM) − 1, where PM is afternoon and AM is morning. Pk_1 and Pk_2 are dominant spectral peaks 1 and 2.

jagged edges or stones often are observed to cause bubble breakup and tearing. Over a wide range of gas fluxes, the bubble distribution remains unchanged (only the bubble emission rate changes); however, if the flux is high enough, small bubbles are formed, or bubbles coalesce immediately after escaping the vent mouth [*Leifer and Boles*, 2004].

[32] One possible mechanism by which swell could influence seep flux is by the associated horizontal motions along the seabed. These motions were clearly visible in underwater video from the motion of suspended detritus. Bubble formation from a vent (or capillary tube) involves the rupturing of the interface at the vent mouth. If the water flow pushes the forming bubble to one side, the bubble "necks" easier when pinching-off, decreasing the bubble size, although the effect is negligible for low water flow velocities [*Tsuge et al.*, 1981]. The water flow also helps break off the bubbles, decreasing resistance to bubble formation. However, since the tent skirts roughly were "sealed" to the seabed, vents covered by the tents were unlikely to experience any effects from swell-induced lateral flow motions.

[33] A rough sketch of the Shane Seep sediment overburden is shown in Figure 11, which explains why it is appropriate to discuss fractures in sediment. The thickness of the tar mix was based on a single push core. The tar mix layer was collected and analyzed and is predominantly tar and sand, but included other organic material [*La Montagne et al.*, 2004]. The tar mix is very cohesive, ~30 cm thick, and overlays a sandy layer. Fractures (pathways of lower resistance, or higher elasticity) extend through the tar mix and are quasi-permanent features. For example, rebars were placed at several vent openings to identify the vent openings in subsequent surveys. Some of these vents persisted several years [*Leifer et al.*, 2004]. Thus, explaining bubble emissions from persistent vents requires fractures, i.e., stable points, rather than random points on the seabed. Pathways through the sand may be random or quasi-random, while the orientation of the major vents along an east-west line and the apparent organization of many vents into lines suggests control from fractures in the underlying rock, which are themselves organized along folds and faults.

[34] Bubble formation depends upon several factors, summarized in Figure 11. First, the bubble formation criterion, where the fracture pressure, P_F, must be greater than the combined hydrostatic pressure, P_H, and La Place pressure, P_{ST}, from the surface tension force. For low flow, the time to form a bubble depends simply on the flow in the fracture and the emitted bubble's volume, which is solely dependent on fracture mouth size. Thus any process that changes the flow, the bubble size, or P_H will change the bubble emission rate or seep gas flux. At higher P_H it takes longer to "blow" a bubble than at lower P_H. However this

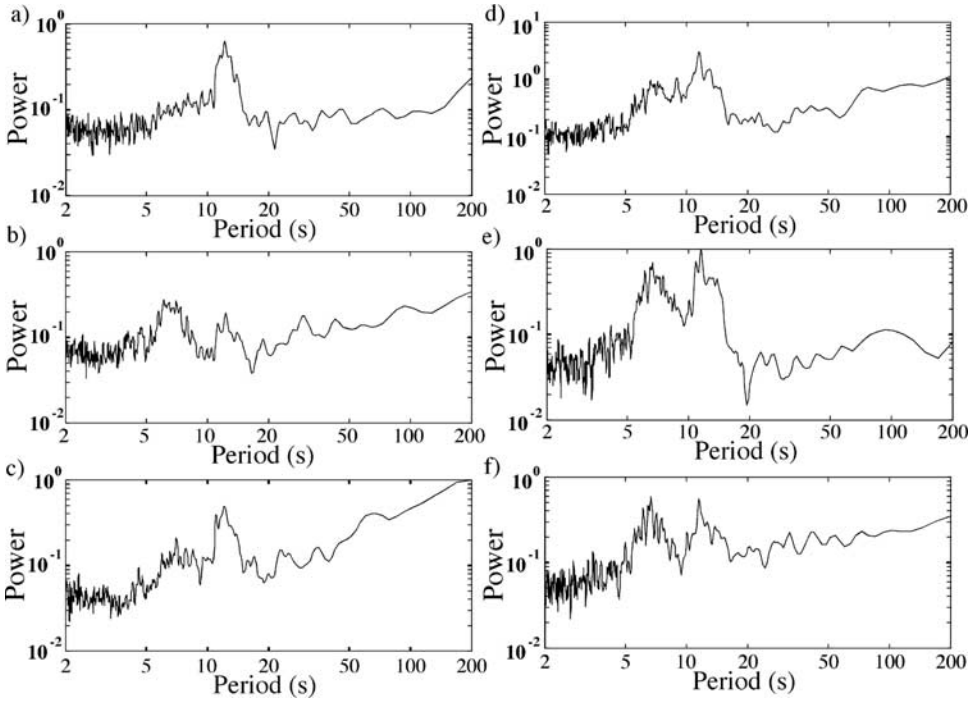

Figure 9. Power spectra (in L s^{-1} Hz^{-1}) for flow from Tents 1, 2, and 3 in (a–c) morning and (d–f) afternoon. See text for details.

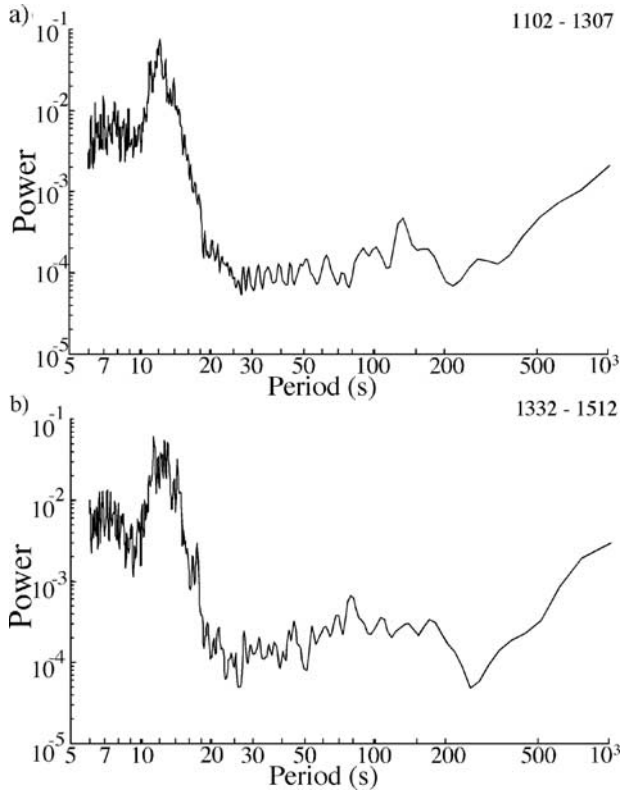

Figure 10. Power spectra from the seabed pressure sensor at Shane Seep in (a) morning, 1102–1307 LT, and (b) afternoon, 1332–1512 LT.

effect does not produce amplification, since by Boyle's law, the bubble volume is related linearly to pressure ($P_1/P_2 = V_2/V_1$).

[35] Thus we propose several possible mechanisms that may be important to explaining how swell induced hydrostatic pressure, P_H, variations could affect seepage. The first is based on pore activation and deactivation (pore activation mechanism) as proposed by *Boles et al.* [2001]. The second mechanism is that the sediment surrounding the fracture adsorbs or desorbs gas depending upon P_H, termed "gas charging." The third mechanism is that fracture size is affected by changes in P_H, termed "fracture forcing." All mechanisms likely occur; however, we believe pore activation is dominant.

4.1. Pore Activation

[36] In the real world, a seep area contains numerous vents spanning many sizes and connectivity paths (or resistances). As the downward portion of swell causes the pressure at the seabed to drop, fractures begin to flux faster, which decreases P_F until equilibrium is restored. However, due to fracture resistance, P_F may not drop as fast as P_H, and thus currently inactive vents become active once the bubble formation criterion is exceeded. The newly activated vents cause P_F to decrease more rapidly. Thus pore activation continues until near equilibrium is restored. Conversely, an increase in P_H has the opposite effect, deactivating pores. Generally, the pores that are activated and deactivated are the smaller ones as they have higher flow resistance and surface tension from their smaller bubbles. Thus, for a given variation in hydrostatic pressure (at the seabed), pore activation amplifies this "input," causing a much larger variation in the flux. In an extreme example, if all vents are deactivated for some of the swell cycle an extremely large amplification would result. This cyclical activation/deactivation was observed for the lowest flux vents (vents that produce single bubble line streams) in video obtained by the divers, although it also appeared correlated with horizontal swell motions.

[37] The pore activation mechanism exhibits a phase lag as the system is always trying to "catch up" to the swell with the maximum flux occurring slightly after the lowest P_H. If a P_H change occurs slowly enough, the system (i.e., P_F) responds concurrently with P_H and there is no amplification. At what frequency the system can respond depends upon the flux, the fracture resistance, and thus the effective fracture volume that responds to surface pressure variations. Clearly, deep portions of the fractures are disconnected from the equilibration process. For more active vents, pore activation amplification is less because P_F more closely follows P_H, (i.e., the timescale for the fracture volume to adjust is less because of the higher flow rate).

4.2. Gas Charging

[38] If the fractures are not in rock, but sediment, the volume of the near seabed subsurface "fracture reservoir" includes the sediment surrounding the fractures. In steady state, the fractures are in Henry's Law equilibrium with the sediment surrounding the fracture (note P_H increases with sediment depth). However, a decrease in P_H causes the sediment to become supersaturated and gas diffuses from the sediment into the bubbles in the fractures, increasing the gas flow. Increasing P_H has the opposite effect. Maximum gas charging occurs when P_H is changing fastest, i.e., there

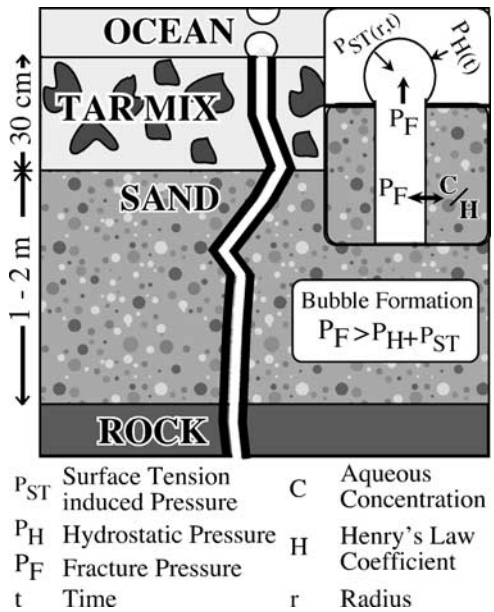

Figure 11. Schematic showing sediment overburden layers, and processes relevant to the mechanism by which pressure variations affect seep gas flux. Symbols defined on figure.

is a 90° phase lag shift, and the ability of the sediment to adsorb (or desorb) gas depends upon the diffusivity of the gas through the sediment. If the change in P_H is very slow, the sediment will remain very close to Henry's Law equilibrium and there will not be an effect. To first order, the gas charging mechanism is independent of the gas flux, so the variation it can cause decreases linearly with increasing flow.

4.3. Fracture Forcing

[39] The flow rate likely is affected if the resistance changes, i.e., if the fracture dimensions vary. In this model, a swell induced increase in P_H forces water into the fractures, enlarging them and thereby decreasing flow resistance and increasing the flux. This "forcing" is most likely for shallow fractures in the sediment near the seabed (tar and sand, not rock), decreasing with depth below the seabed. Since we assume the sediment mechanical response is very quick, the phase lag should be small, i.e., peak flow occurs at peak P_H when the fractures are the most open. The effect should decrease with increasing fracture cross section and thus be strongly fracture-size dependent.

4.4. Mechanism Comparison

[40] Of these three mechanisms, the smallest contribution is likely from gas charging. Not only is the tar-mix sediment largely impermeable, but also the amplification factor was much greater than one (i.e., nonlinear). Moreover, the flow rates were very high, on the order of many liters per second, and it is hard to envision diffusion producing variations of up to 4% in less than half the wave period (~3 s). In contrast, both fracture forcing and pore activation are consistent with a decreased response (i.e., amplification) for higher flow vents since they have lower resistance and thus a larger cross section. Tents with greater flux showed less variation at swell frequencies than lower flux tents.

[41] The mechanism must also explain the observed response of the seep flow at the different swell frequencies. For example, the NOAA wave-buoy wave spectra had more power in the 7 s than the 12 s spectral peak in the afternoon (Figure 10); a comparison between 7 s and 12 s power levels for the CTD spectra is unreliable because of the instrument sampling frequency. However, for all tents, the spectral peak in the flux for 7 s was at most comparable (Tents 2 and 3) or significantly smaller (Tent 1) than the 12 s peak. We propose this is best explained by the pore activation mechanism since it implies a strong phase lag based on the system response. For very slow P_H changes, there is no phase lag (the system adjusts and remains in equilibrium) and the flux is independent of P_H. If P_H changes too fast for the system to respond, the flux remains in equilibrium with the mean. The pore activation mechanism can explain very high amplification of swell-induced pressure variations due to the phase lag.

[42] Thus it was doubly unfortunate that the CTD internal data logger required manual synchronization with the Omega data logger (i.e., ±1 s). As a result, the time precision was insufficient to measure the phase lag of the dominant 7-s period wave and tent response. The trend in the standard deviations of the fluxes for Tents 2 (smallest) and 1 (largest) shown in Table 1, is consistent with both the "pore activation" and "fracture forcing" models since both predict a smaller effect for larger fractures (i.e., lower resistance or higher flow) vents. Note that by fracture size, we mean a flux-weighted average fracture size under each tent. In other words, the presence of larger fractures and pores led to a decreased sensitivity of the vents to pressure fluctuations. This relationship is apparent in the spectra. The greatest dissimilarity between morning and afternoon spectra was for Tent 2 (Figures 9b and 9e) where the 7 s peak was stronger than the 12 s peak in the morning but was weaker in the afternoon. The greatest similarity in spectra between morning and afternoon was for Tent 1 (Figures 9a and 9d) where the 12 s peak was dominant both in the morning and afternoon.

[43] The stronger response at the 12 s period than the 7 s period for Tent 1 (Figures 9a and 9d) could be explained if the vent system was able to respond to the 12 s swell forcing, but has difficulty responding to the shorter 7 s swell. However, interpretation of the spectra is unclear. While Tents 1 and 2 showed a greater increase in the 12 s response than the 7 s response, Tent 3 showed the opposite.

[44] Spectral components of the seep-tents clearly changed from morning to afternoon, during which time there were significant changes not only in the swell, but the water temperature (~1°C, from the change in tidal currents), tidal depth (~30 cm, i.e., ~30 mbar), and atmospheric pressure (~3 mbar). Although clearly none varied significantly on the timescale of the swell, they could affect the seep response to swell. For example, given the low thermal conductivity of sediments, a thermal mechanism could result from seawater recirculation flow back into the seep fracture network. In that case, the colder (or warmer) water flow causes the sediment surrounding the fracture to shrink (or expand), increasing (or decreasing) resistance and affecting the flow. A recirculation flow driven by the bubbles flowing through pathways in unconsolidated sediment was observed in the laboratory [*O'Hara et al.*, 1995]. Furthermore, there is evidence of a seawater recirculation flow down one kilometer to the hydrocarbon reservoir [*Boles et al.*, 2004]. To affect seepage at Shane Seep a recirculation flow need only penetrate a few meters to tens of meters. A requirement for this thermal mechanism is that the fractures are very narrow.

[45] During the day, the increase in hydrostatic pressure from the tide and atmospheric changes increases the load on the seabed sediments. This should compress fluid into the fractures (in unconsolidated sediment) thereby enlarging them, i.e., the fracture forcing mechanism, and affecting the response of the pore activation mechanism.

[46] Finally, it is important to note that the hydrocarbon flux through these vents is not just natural gas and water, but includes oil and tar. Since it is unlikely that the oil to gas ratio is the same in different vents, the flow resistance (viscosity) of the different phases suggests fractionation is likely, a pattern observed in the COP seep field as a whole (Shane Seep has the highest gas flux and is the gassiest, i.e., highest gas to oil ratio, while less active seeps, i.e., Farrar Seep, are oilier). The presence of oil

allows for a complex temporal response to both transient and cyclical forcing, including processes related to fracture blockage and blow-through, slug flow, wettability, and the interpermeability of the phases [*Leifer et al.*, 2004]. For example, oil viscosity is temperature sensitive, suggesting a decreased oil flow with decreased temperature (from the recirculation flow described above). The decreased oil flow would then fill the fractures more, increasing resistance to the flow of gas. The increased resistance then causes a rise in internal pressure (which increases the gas flow) until a new equilibrium is reached. This new equilibrium could involve a shifting of the flow toward less oily fractures, i.e., deactivation of oilier fractures with decreasing temperature and activation with increasing temperature.

[47] These data at a shallow (22 m) seep show that seeps respond at swell frequencies, i.e., on the order of a 10-s timescale. At even shallower seeps the swell forcing on seep flux should be greater. This was noted during seep-tent studies to quantify the oil and gas flux in very shallow (5 m) water, off Summerland, California (K. Wilson CADFG, OSPR, personal communication, 2003). For deeper seeps, the amplification observed suggests that the swell effect should be observable at seeps 100–200 m deep. For example, 4-m swell should produce a 0.9% flux emission variation for vents such as under Tent 2 at 200 m. Naturally, this effect would extend deeper and be significantly larger during storms.

[48] We would like to note that while these variations are not in and of themselves of significance to estimating total flux, they present an approach to study the subsurface mechanisms that control seepage.

5. Conclusion

[49] In this paper, we presented a detailed description of a new and inexpensive approach to measuring seep flux, a turbine seep-tent, which can be deployed to any depth. Limitations might include hydrate deposition on the turbines for methane seeps in the hydrate stability zone and mineral deposition for black smokers. Since the data are highly compressible, long-term records with very high temporal resolution are possible. The inexpensive design allows construction of more units. This paper shows the value of a multiple tent network in allowing a comparison of the frequency response to external forcing (swell) for different fluxes. The tent network used simultaneous measurements to study hydrocarbon migration in near-seabed subsurface fractures.

[50] The system was deployed successfully on 11 March 2003 and recorded fluxes at three different areas in an active seep area, Shane Seep. Data analysis clearly showed a frequency-dependent, flux response at swell frequencies, including the increase in swell with the worsening weather during the day. On the basis of the seep frequency response, we propose that the dominant controlling mechanism was pore activation. For different seeps where the sediment overburden and fracture structure differ, other mechanisms may be dominant.

[51] One problem with the current tent design was quantization and poor counting statistics at the desired time resolution (<1 s). A more recent tent version uses optical encoders instead of Hall Effect sensors that generate 100 pulses per revolution. This significantly improves the statistics and thus the effective minimum time resolution achievable for typical seep fluxes. Encoders with even greater numbers of pulses per rotation are available if data with even higher time resolution is required.

[52] **Acknowledgments.** We would like to thank the support of the University of California Energy Institute, and the U.S. Mineral Management Service, Agency 1435-01-00-CA-31063, Task 18211. Special thanks to UCSB divers, Shane Anderson, Dave Farrar, Dennis Divins, and underwater videographer, Eric Hessel. Special thanks to Una Matko and Tom Carpenter for their work in tent construction and calibration.

References

Allen, A. A., R. S. Schlueter, and P. G. Mikolaj (1970), Natural oil seepage at Coal Oil Point, Santa Barbara, California, *Science*, *170*, 974–977.

Blanchard, D. C., and L. D. Syzdek (1977), Production of air bubbles of a specified size, *Chem. Eng. Sci.*, *32*, 1109–1112.

Boles, J. R., J. F. Clark, I. Leifer, and L. Washburn (2001), Temporal variation in natural methane seep rate due to tides, Coal Oil Point area, California, *J. Geophys. Res.*, *106*, 27,077–27,086.

Boles, J. R., P. Eichhubl, G. Garven, and J. Chen (2004), Evolution of a hydrocarbon migration pathway along a basin bounding fault, *AAPG Bull.*, *88*(7), 947–970.

Chen, R. C., J. Reese, and L.-S. Fan (1994), Flow structure in a three-dimensional bubble column and three-phase fluidized bed, *AIChE J.*, *40*(7), 1093–1104.

Clark, J. F., L. Washburn, J. S. Hornafius, and B. P. Luyendyk (2000), Dissolved hydrocarbon flux from natural marine seeps to the southern California Bight, *J. Geophys. Res.*, *105*, 11,509–11,522.

Clark, J. F., I. Leifer, L. Washburn, and B. P. Luyendyk (2003), Compositional changes in natural gas bubble plumes: Observations from the Coal Oil Point Seep Field, *Geo Mar Lett.*, *23*, 187–193.

Clester, S. M., J. S. Hornafius, J. Scepan, and J. E. Estes (1996), Quantification of the relationship between natural gas seepage rates and surface oil volume in the Santa Barbara Channel, *EOS Trans. AGU*, *77*(46), Fall Meet. Suppl., F420.

Fan, L.-S., and K. Tsuchiya (1990), *Bubble Wake Dynamics in Liquids and Liquid-Solid Suspensions*, 363 pp., Butterworth-Heinemann, Woburn, Mass.

Fischer, P. J. (1978), Natural gas and oil seeps, Santa Barbara Basin, California, in *California Offshore Gas, Oil, and Tar Seeps*, pp. 1–62, State of Calif. State Lands Commission staff report, Sacramento.

Hills, J. H. (1974), Radial non-uniformity of velocity and voidage in a bubble column, *Trans. Inst. Chem. Eng.*, *52*, 1–9.

Hornafius, J. S., D. C. Quigley, and B. P. Luyendyk (1999), The world's most spectacular marine hydrocarbon seeps (Coal Oil Point, Santa Barbara Channel, California): Quantification of emissions, *J. Geophys. Res.*, *104*, 20,703–20,711.

Khalil, M. A. K., and R. A. Rasmussen (1995), The changing composition of the Earth's atmosphere, in *Composition, Chemistry, and Climate of the Atmosphere*, edited by H. B. Singh, pp. 50–87, Van Nostrand Reinhold, New York.

Kvenvolden, K. A., W. S. Reeburgh, and T. D. Lorenson (2001), Attention turns to naturally occurring methane seepage, *Eos Trans. AGU*, *82*(40), 457.

La Montagne, M. G., I. Leifer, S. Bergmann, L. C. Vandewerfhorst, and P. A. Holden (2004), Bacterial diversity in marine hydrocarbon-seep sediments, *Environ. Microbiol.*, *6*(8), 799–808.

Leifer, I., and J. Boles (2004), Measurement of hydrocarbon flow through fractured rock and unconsolidated sediment of a marine seep, *Mar. Pet. Geol.*, in press.

Leifer, I., and R. Patro (2002), The bubble mechanism for transport of methane from the shallow sea bed to the surface: A review and sensitivity study, *Cont. Shelf Res.*, *22*, 2409–2428.

Leifer, I., J. Clark, and R. Chen (2000), Modifications of the local environment by a natural marine hydrocarbon seep, *Geophys. Res. Lett.*, *27*(22), 3711–3714.

Leifer, I., J. Boles, J. F. Clark, and B. Luyendyk (2004), Transient discharges from marine hydrocarbon seeps: Spatial and temporal variability, *Environ. Geol.*, *46*(8), 1038–1052.

O'Hara, S. C. M., P. R. Dando, U. Schuster, A. Bennis, J. D. Boyle, F. T. W. Chui, T. V. J. Hatherell, S. J. Niven, and L. J. Taylor (1995), Gas seep induced interstitial water circulation: Observations and environmental implications, *Cont. Shelf Res.*, *15*, 931–948.

Prather, M., R. Derwent, D. Ehhalt, P. Fraser, E. Sanhueza, and X. Zhou (1995), Other trace gases and atmospheric chemistry, in *Climate Change 1994: Radiative Forcing of Climate Change and an Evaluation of the IPCC IS92 Emission Scenarios*, edited by J. T. Houghton et al., pp. 73–126, Cambridge Univ. Press, New York.

Tryon, M. D., K. M. Brown, M. E. Torres, A. M. Trehu, J. McManus, and R. W. Collier (1999), Measurements of transience and downward fluid flow near episodic methane gas vents, Hydrate Ridge, Cascadia, *Geology*, *27*(12), 1075–1078.

Tsuge, H., S. Hibino, and U. Nojima (1981), Volume of a bubble formed at a single submerged orifice in a flowing liquid, *Int. Chem. Eng.*, *21*(4), 630–636.

J. Boles, Department of Geological Sciences, University of California, Santa Barbara, CA 93106, USA.

I. Leifer, Marine Sciences Institute, University of California, Santa Barbara, CA 93106, USA. (ira.leifer@bubbleology.com)